



# Enhanced Microstructural Stability and Hardness of Multi-component Nanocrystalline Nickel Alloys Processed *via* Mechanical Alloying

MARI-THERESE S. BURTON, B. CHAD HORNBuckle, VINCENT H. HAMMOND, KRISTOPHER A. DARLING, HELEN M. CHAN, CHRISTOPHER J. MARVEL, and MARTIN P. HARMER

Nanocrystalline alloys are noteworthy for their high strength, and nanocrystalline Ni is being investigated for high-temperature applications. However, nanocrystalline alloys are unstable against coarsening, thereby prone to degradation of strength. In this work, two nanocrystalline alloys, Ni-(0, 11 at pct W)-3 at pct Ta-2 at pct Y, were designed to exhibit microstructural stability and high strength by forming nanoscale precipitates, maintaining stable nanoscale grains to exploit Hall-Petch hardening, and decreasing the stacking fault energy of the Ni-based matrix. Produced *via* high-energy cryogenic mechanical alloying, both alloys exhibited thermal stability and enhanced mechanical properties due to beneficial impurity yttrium oxide/nitride particles and argon bubbles that pin grain boundaries. Hardness testing and advanced characterization techniques, namely scanning transmission electron microscopy, were used to elucidate microstructure-property relationships. The difference in impurity ceramic phase affected the alloys' relative stability and hardness. The Ni-11W-3Ta-2Y alloy with Y<sub>2</sub>O<sub>3</sub> nanoparticles was even more stable and harder than the Ni-3Ta-2Y alloy with YN particles, maintaining nanoscale grains after annealing at 70 pct homologous temperature for 100 hours and demonstrating hardness enhanced by over 2 GPa above the Hall-Petch contribution. The yttrium oxide/nitride particles, Ni<sub>3</sub>Y intermetallic phase, and pure artifact W/Ta grains remaining from milling, play a role in the enhanced hardening.

<https://doi.org/10.1007/s11661-024-07328-5>

© The Minerals, Metals & Materials Society and ASM International 2024

## I. INTRODUCTION

NEW materials with high strength and ductility at high temperatures are needed for elevated temperature applications, such as jet engine turbine blades and power plants. Materials used for such applications must be able to withstand applied stresses at such temperatures without plastically deforming over extended periods of time, so high-temperature strength and creep resistance are essential. Impeding dislocation motion is essential to

increasing strength, at both room temperature and elevated temperatures. There are multiple ways that this can be achieved in alloy design including the classical strengthening mechanisms of grain size refinement,<sup>[1,2]</sup> precipitation hardening, and solid-solution strengthening, as well as by selection of solutes to decrease stacking fault energy, favoring the formation of partial dislocations and twins, which inhibits dislocation motion and cross-slip.<sup>[3]</sup>

Nanocrystalline metals are known for their exceptional strength due to Hall-Petch hardening and their ultra-fine grain sizes.<sup>[4]</sup> However, due to their large volume fraction of grain boundaries, they experience a large driving force for grain growth, which is only exacerbated with temperature due to kinetics. Many pure nanocrystalline metals undergo significant grain growth at and near room temperature. For example, Hibbard *et al.* reported that pure nanocrystalline Ni coarsened from an average grain size of 20 to 350 nm after annealing at 420 °C (40 pct  $T_m$ ) for only 30 seconds; within only 5 days of annealing at 420 °C, grain diameters were in the 20 to 60  $\mu\text{m}$  range.<sup>[5]</sup> Stabilizing nanocrystalline materials against grain growth is

---

MARI-THERESE S. BURTON, HELEN M. CHAN, and MARTIN P. HARMER are with the Department of Materials Science and Engineering, Lehigh University, 5 East Packer Avenue, Bethlehem, PA, 18015. B. CHAD HORNBuckle, VINCENT H. HAMMOND, and KRISTOPHER A. DARLING are with the Science of Extreme Materials Division, DEVCOM Army Research Lab, APG, Aberdeen, MD 21005. CHRISTOPHER J. MARVEL is with the Department of Mechanical and Industrial Engineering, Louisiana State University, 3290J Patrick F. Taylor Hall, Baton Rouge, LA, 70803. Contact e-mail: cmarvel@lsu.edu

Manuscript submitted July 3, 2023; accepted January 16, 2024.

Article published online March 4, 2024

necessary for their favorable mechanical properties to be useful in structural applications.

Binary and ternary nanocrystalline systems have been investigated for their thermal stability against grain growth under various annealing conditions, and alloy design criteria have been suggested to stabilize the nanocrystalline microstructures. One strategy is to thermodynamically limit coarsening *via* grain boundary segregation to decrease grain boundary excess energy,<sup>[6–10]</sup> or to stabilize sluggish grain boundary complexions that have low grain boundary mobility.<sup>[11–15]</sup> Alternatively, nanocrystalline materials can also be stabilized kinetically through the solute drag of grain boundary segregants<sup>[16,17]</sup> and grain boundary pinning.<sup>[18–22]</sup> One well-studied nanocrystalline system which has demonstrated remarkable stability against grain growth in addition to creep resistance is mechanically alloyed copper tantalum,<sup>[19–24]</sup> in which highly stable Ta-based nanoclusters play a grain boundary-pinning role.<sup>[24]</sup>

Many thermally stable nanocrystalline systems are studied after long-term anneals (multiple days) but at relatively low temperatures (30 to 50 pct  $T_m$ ),<sup>[8,12]</sup> while many others are studied after higher temperature anneals (60 to 80 pct  $T_m$ ) but shorter times (1 to 10 hours).<sup>[9,10,14,19,22]</sup> Complexion-stabilized systems have been studied, and remained nanocrystalline, following long-term, high temperature anneals.<sup>[11,15]</sup> In the present work, kinetics-based stability of a nanocrystalline material is demonstrated after annealing at a high temperature (70 pct  $T_m$ ) for a relatively large amount of time (100 hours). Further, the thermal stability of the nanocrystalline structure was only the first of two goals in this work; this microstructural stability enables mechanical stability of high hardness that is promoted by a combination of strengthening mechanisms: Hall–Petch strengthening, solid-solution strengthening, and dispersion hardening from intentional impurity phases. The effects of dispersion and precipitation hardening coupled with solid-solution strengthening have been well studied in coarser-grained systems. For example, in ODS austenitic steels, the introduction of nanoscale dispersoids throughout micron-scaled grains significantly increases strength compared to austenitic steels with no dispersoids<sup>[25]</sup> due to the looping of dislocations around the hard, incoherent dispersed oxide particles. The alloy studied here aims to enhance Hall–Petch strengthening, which is highly effective in nanostructured materials, *via* solid-solution strengthening and dispersion strengthening from intentional impurity phases, which has been shown to significantly strengthen coarse-grained systems like ODS steels.

Because the ultimate goal of the new alloys designed in this study is to remain strong even at elevated temperatures and thermally stable against grain growth, the Cu–Ta system<sup>[20–24]</sup> was considered as an inspiration for the desired microstructure. Nickel, rather than copper, was selected as the primary component in order to increase the working temperature range. The limited intersolubility and large atomic size difference are important to the formation and stability of the grain boundary-pinning nanoclusters in the Cu–Ta system, so

for this new system, dopants with limited solubility in Ni and large atomic size mismatch were selected.

Yttrium is immiscible in Ni with a solubility limit of only 0.1 at pct<sup>[26]</sup> and has a much larger atomic size than Ni.<sup>[26–29]</sup> It is expected to bond with impurities such as nitrogen and oxygen, segregate to grain boundaries, and form nanoscale-pinning particles similar to the Ta-oxide nanoclusters in the Cu–Ta system. A small alloying addition, 2 at pct Y, was selected to promote the formation of Y-based pinning particles but avoid formation of potentially deleterious intermetallic phases.

When dissolved in coarse-grained Ni, Ta and W have been shown to improve high-temperature mechanical properties, namely strength and creep. Both of these components impede dislocation motion when in solid solution, decrease the stacking fault energy<sup>[30,31]</sup> (which promotes the formation of partial dislocations and twins), and increase the activation energy for lattice diffusion (which decreases the steady-state creep rate).<sup>[3]</sup> These effects are expected to be maximized by increasing the amount of W dissolved in Ni, so, to maximize its effects but avoid forming intermetallic phases, 3 at pct Ta and 11 at pct W (the solubility limit of W in pure Ni at 600 °C) was selected for the nominal composition.<sup>[26]</sup>

## II. METHODS/EXPERIMENTAL PROCEDURES

### A. Material Processing

Two alloys, with nominal compositions of 95 at pct Ni–3 at pct Ta–2 at pct Y, and 84 at pct Ni–11 at pct W–3 at pct Ta–2 at pct Y were cryogenically mechanically alloyed from elemental powders in a high-energy shaker mill. The powders were sourced from Alfa Aesar with the following specifications: Ni: – 325 mesh and 99.8 pct metal basis, W: – 325 mesh and 99.9 pct metal basis, Ta: – 325 mesh and 99.97 pct metal basis, and Y: – 40 mesh and 99.6 pct metal basis. To limit contamination, powders were loaded into nickel vials with nickel milling media inside of an argon-filled glovebox, with a ball to powder ratio of 10:1. The modified SPEX 8000 M mill was cooled using liquid nitrogen or liquid argon. Powders were milled for 8 hours, resulting in powder particle sizes ranging from 10 to 50  $\mu\text{m}$ . The as-milled powder was compacted into 3-mm-diameter pellets by uniaxial pressing at 3 GPa in a tungsten carbide die, and then pellets were annealed at temperatures ranging from 400 to 1000 °C for 1, 10, and 100 hours in an inert argon atmosphere.

### B. Hardness Testing

Vickers microhardness measurements were performed on polished as-milled and annealed compacts using a Buehler Tukon 1202 hardness indenter. A load of 50 g was used with a dwell time of 10 seconds per indent, collecting at least 25 indents per sample that were observed to not intersect with any pores. Error bars were calculated as 95 pct confidence intervals based on a

normal distribution. Indents were placed near the center of particles to avoid effects due to inter-particle voids and surfaces.

### C. Microstructural Characterization

Transmission electron microscopy (TEM) samples were prepared for microstructural characterization using the *in situ* focused ion beam (FIB) method in an FEI Scios or ThermoFisher Helios G4 UX Dual Beam FIB/SEM. Energy-dispersive spectroscopy (EDS) was performed in the FIB/SEM using an EDAX Ametek silicon drift EDS detector. TEM specimens were milled out of the as-milled and annealed samples, avoiding inter-particle voids, attached to Mo or Cu TEM grids, and thinned using a 30 kV Ga ion source. The accelerating voltage of the ion source was decreased to 5 kV for the final FIB-thinning step, and then polished using a Fischione 1040 Nanomill with a 900 eV Ar ion source to remove damage and Ga implantation from the FIB process.

Both conventional TEM and aberration-corrected scanning TEM (ac-STEM) were performed using a JEOL JEM-2100 instrument and a JEOL ARM-200CF instrument or JEOL 2100F instrument, respectively, both operated at 200 kV. Selected area electron diffraction (SAED) patterns were acquired using the 100  $\mu\text{m}$  selected area aperture in the JEOL JEM-2100 TEM. Bright field (BF), low-angle annular dark field (LAADF), and high-angle annular dark field (HAADF) ac-STEM images were collected. Spatially resolved EDS measurements were collected using a JEOL Centurio 100  $\text{mm}^2$  silicon drift detector mounted in the ARM-200CF.

## III. RESULTS

The Ni-3Ta-2Y samples were milled first, using liquid nitrogen as the cryogen, and they were found to have significant amounts of nitride impurities, so liquid argon was used for cryomilling the Ni-11W-3Ta-2Y samples instead. Because of these impurities, the Ni-11W-3Ta-2Y alloy was investigated in more depth, and the Ni-3Ta-2Y samples were primarily considered as a reference material. For both compositions, the as-milled samples were nanocrystalline with regions of unmilled nickel, tantalum, and tungsten (for the Ni-11W-3Ta-2Y sample). They may contain some amorphous phases due to the high-energy input during the mechanical alloying process. Representative cropped SAED patterns of as-milled and annealed samples and a full SAED pattern, Azimuthal projection, and accompanying crop of the SAED pattern for the 800 °C 1-hour-annealed Ni-11W-3Ta-2Y sample are presented in Figure 1. All visible spots or rings are labelled, and the full SAED patterns and Azimuthal projections for the cropped SAED patterns from Figure 1 can be found in the Appendix, Figure A1. The SAED patterns acquired from as-milled and low-temperature annealed samples contained diffuse rings, indicating presence of very small grains and potentially some amorphous

material. Even in the as-milled state, however, the samples were at most partially amorphous, as evidenced by the crystalline spots observed in the SAED pattern in Figure 1. Phase identification was performed using a combination of SAED patterns and STEM EDS. In addition to the Ni-rich FCC matrix phase, samples contained  $\text{Y}_2\text{O}_3$  based on the presence of the yttria 222 ring in SAED patterns and in STEM EDS measurements.

For identification of phases, STEM EDS and SAED patterns were combined. Representative STEM EDS maps and a STEM HAADF micrograph from the corresponding region of the 800 °C 100 hours annealed sample are shown in Figure 2. In HAADF micrographs, contrast scales with mass thickness, so pixels with higher intensities show either thicker regions of the thin foil or regions with higher average atomic numbers; for example, assuming constant thickness, pure W appears bright while  $\text{Y}_2\text{O}_3$  appears dark. The grain in Figure 2(a) is pure Ta, which is reflected in the elemental maps, where Ta is enriched in that grain only and all other components are depleted. In addition, there is a phase which is enriched in Y and contains some Ni. The intermetallic phase  $\text{Ni}_5\text{Y}$  was identified in SAED patterns. A higher-magnification STEM HAADF micrograph and accompanying STEM EDS maps of this sample which show the presence and morphology of  $\text{Y}_2\text{O}_3$  particles can be found in the Appendix, Figure A2. Similarly, a representative STEM HAADF micrograph and corresponding elemental STEM EDS maps of the Ni-3Ta-2Y sample annealed at 800 °C for 100 hours can be found in Figure 3. In this map, there is a region which is bright in the Y and N maps, indicating that it is enriched in both of these components and is likely a YN particle.

A combination of SAED patterns and STEM EDS was used for phase identification, but STEM HAADF imaging of the as-milled and annealed samples gives further insight into the microstructural evolution of these alloys as they were annealed. Representative STEM HAADF micrographs of Ni-11W-3Ta-2Y samples in the as-milled condition and annealed for 1 hour can be seen in Figure 4. The sample in the as-milled condition and the sample that was annealed at 600 °C for 1 hour were observed to have a large amount of remaining crystalline W and Ta that were not fully mixed during milling and had not dissolved into the Ni phase, as seen by the bright phases in Figures 4(a), (b), (f), and (g). As the annealing temperature increases, these pure, unmixed W and Ta grains constitute a smaller fraction of the microstructure as the W and Ta dissolve into the Ni phase. These W and Ta grains are artifacts from elemental powder particles which were not fully broken down and mixed in during the milling process. Representative STEM HAADF images of Ni-11W-3Ta-2Y and Ni-3Ta-2Y annealed for 100 hours are compared in Figure 5, where pure W is labeled with black squares,  $\text{Ni}_5\text{Y}$  with white triangles,  $\text{Y}_2\text{O}_3$  circled in yellow, and for in the Ni-3Ta-2Y sample, YN is labeled with white diamonds. Based on STEM imaging of samples annealed at 900 °C for 1 and 100 hours (Figures 4(d) and (i), and Figure 5(c) and (f)),

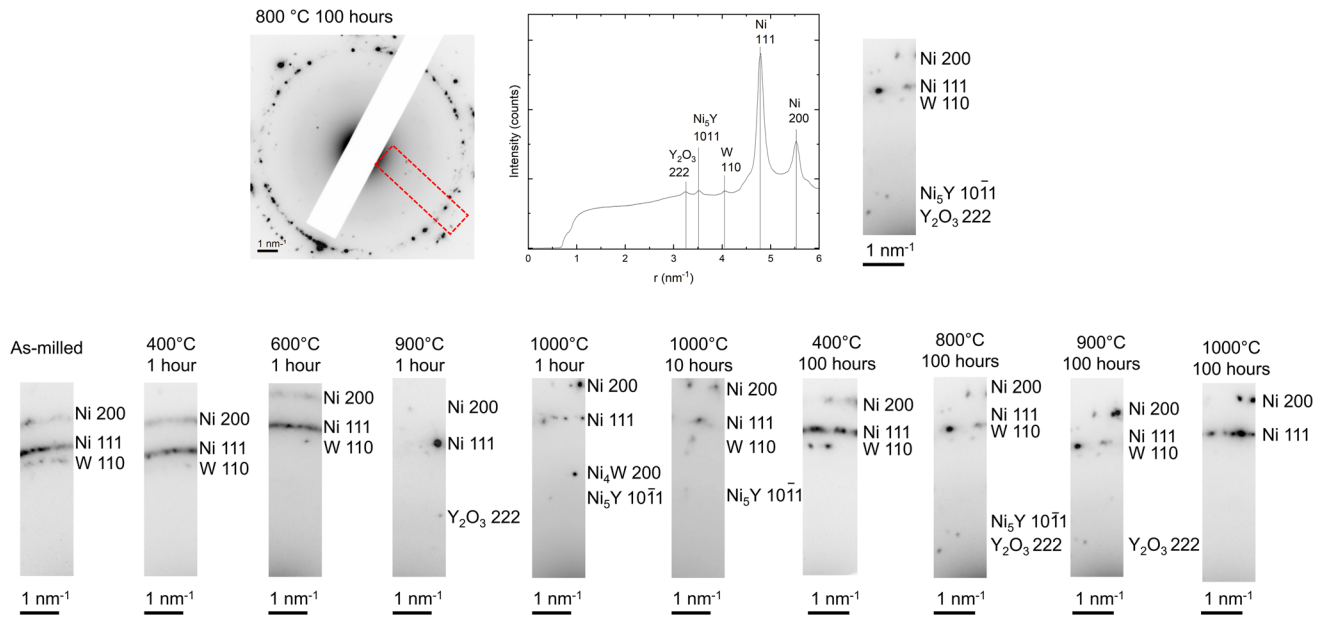


Fig. 1—Representative full SAED pattern, Azimuthal projection, and cropped section of the SAED pattern for the 800 °C 100 hour annealed sample of Ni–11W–3Ta–2Y. This process was repeated for samples in the as-milled and all annealing conditions, and the cropped sections of SAED patterns are included here with rings/spots indexed by phase and family of planes.

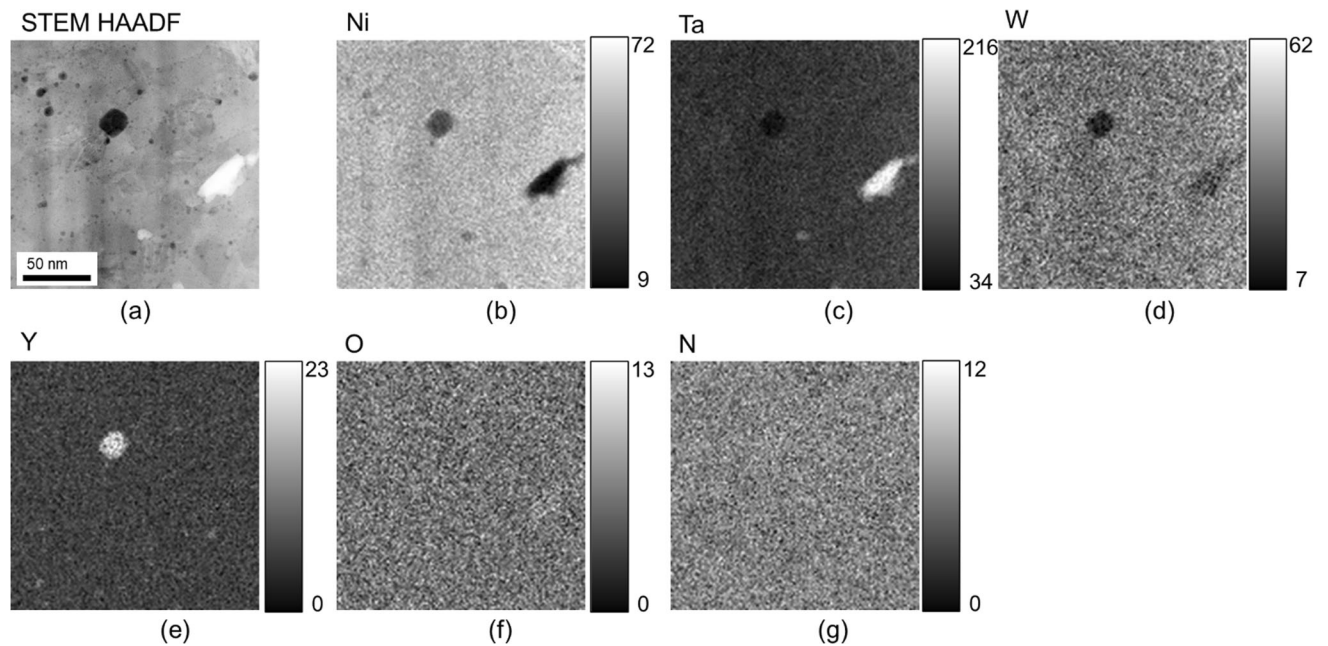


Fig. 2—STEM HAADF micrograph (a) and STEM EDS elemental maps (b through g) of a representative area of the Ni–11W–3Ta–2Y sample annealed at 800 °C for 100 hours. The elemental maps are background-subtracted net count maps. The regions which are bright in the Ta map and dark in all others are enriched in Ta, indicating that they are pure Ta particles. This is consistent with the bright contrast of these grains in the HAADF micrograph. In addition, there is a region that is bright in Y and very dark in the W and Ta maps. This region contains some Ni, but it is depleted compared to the matrix. By combining EDS measurements and SAED patterns, this phase is identified as Ni<sub>5</sub>Y. The surrounding matrix phase is observed to contain Ni, W, and some Ta.

the Y<sub>2</sub>O<sub>3</sub> particles are resistant against coarsening and appear along grain boundaries. More specifically, the mean Y<sub>2</sub>O<sub>3</sub> particle diameter after annealing at 900 °C for 1 and 100 hours was 5.7 ± 2.9 nm and 7.6 ± 4.1 nm, respectively. In addition, argon bubbles

are present, typically at grain boundaries and coupled with the Y<sub>2</sub>O<sub>3</sub> particles. Their mean diameter evolved from 3.3 ± 1.5 nm to 5.8 ± 3.1 nm after annealing at 900 °C for 1 and 100 hours, respectively.

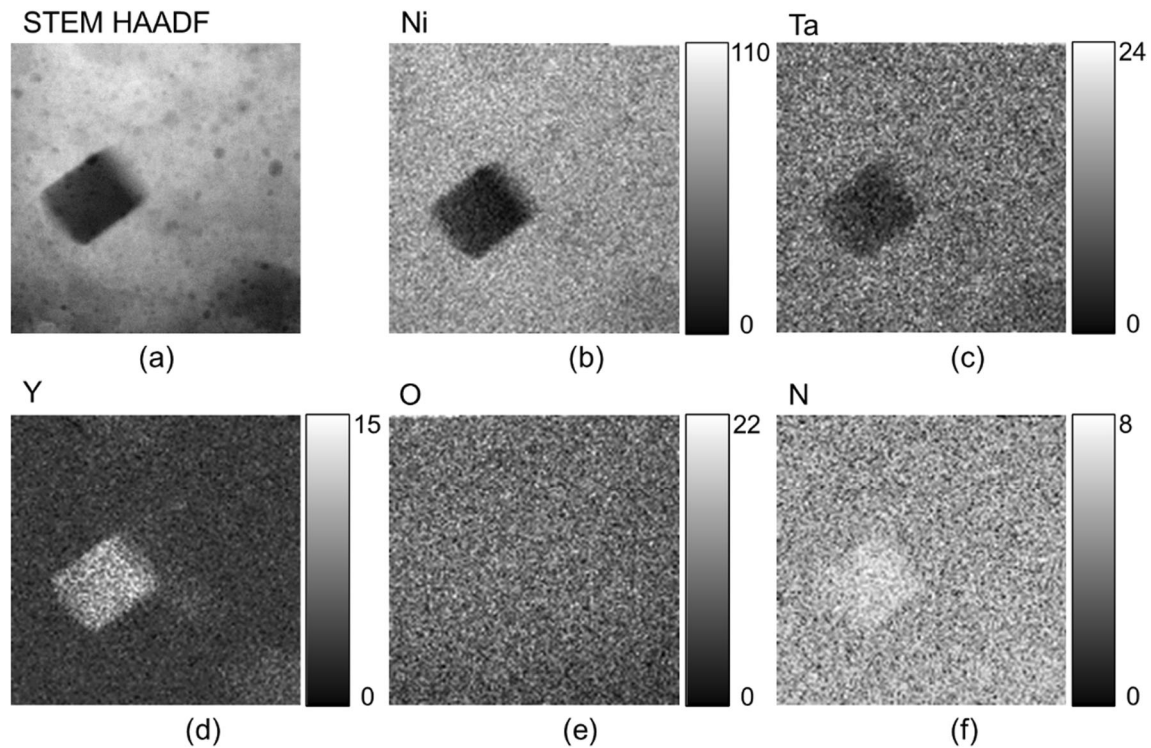


Fig. 3—STEM HAADF micrograph (a) and STEM EDS elemental maps (b through f) of a representative area of the Ni-3Ta-2Y sample annealed at 800 °C for 100 hours. The elemental maps are background-subtracted net count maps. The region which is bright in the N and Y EDS maps, and dark in the Ni and Ta maps, is enriched in both N and Y and depleted in Ni and Ta, indicating that it represents a YN particle. This is consistent with the dark contrast of this particle seen in the corresponding HAADF micrograph. The surrounding matrix phase is observed to contain Ni and Ta.

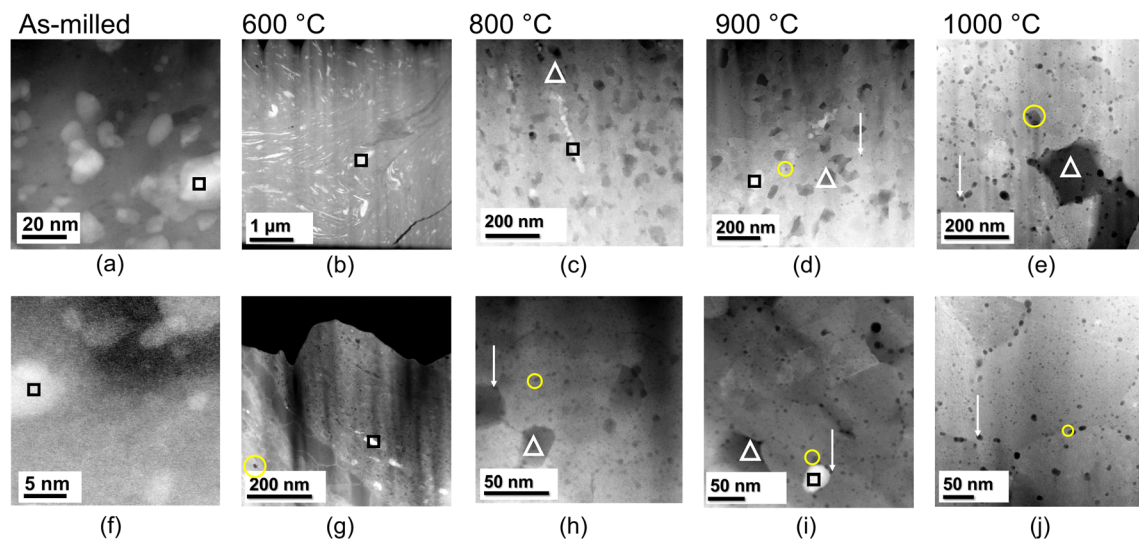


Fig. 4—STEM HAADF images of Ni-11W-3Ta-2Y samples in the as-milled condition (a, f) and after annealing for 1 hour at 600 (b, g), 800 (c, h), 900 (d, i), and 1000 (e, j) °C. Pure W grains are marked with black squares and Ni<sub>5</sub>Y with white triangles. A large Y<sub>2</sub>O<sub>3</sub> particle is circled in yellow, and a large Ar bubble is marked with a white arrow in each image where they are visible.

Figure 6(a) displays the grain/crystallite size of Ni-11W-3Ta-2Y, compared to published literature values for Ni-1Y<sup>[19]</sup> and pure Ni, all annealed for 1 hour.<sup>[6,20,32–34]</sup> Grain sizes of Ni-11W-3Ta-2Y after annealing at selected temperatures for 100 hours are also presented. A line intercept method based on ASTM

Standard E112, Section 13<sup>[35]</sup> was used on STEM HAADF images of Ni-11W-3Ta-2Y to determine grain size. Meanwhile, the reported grain sizes for cryomilled nanocrystalline Ni-1Y from the literature were calculated using the X-ray diffraction line broadening analysis, which neglects the effects of strain and twinning on

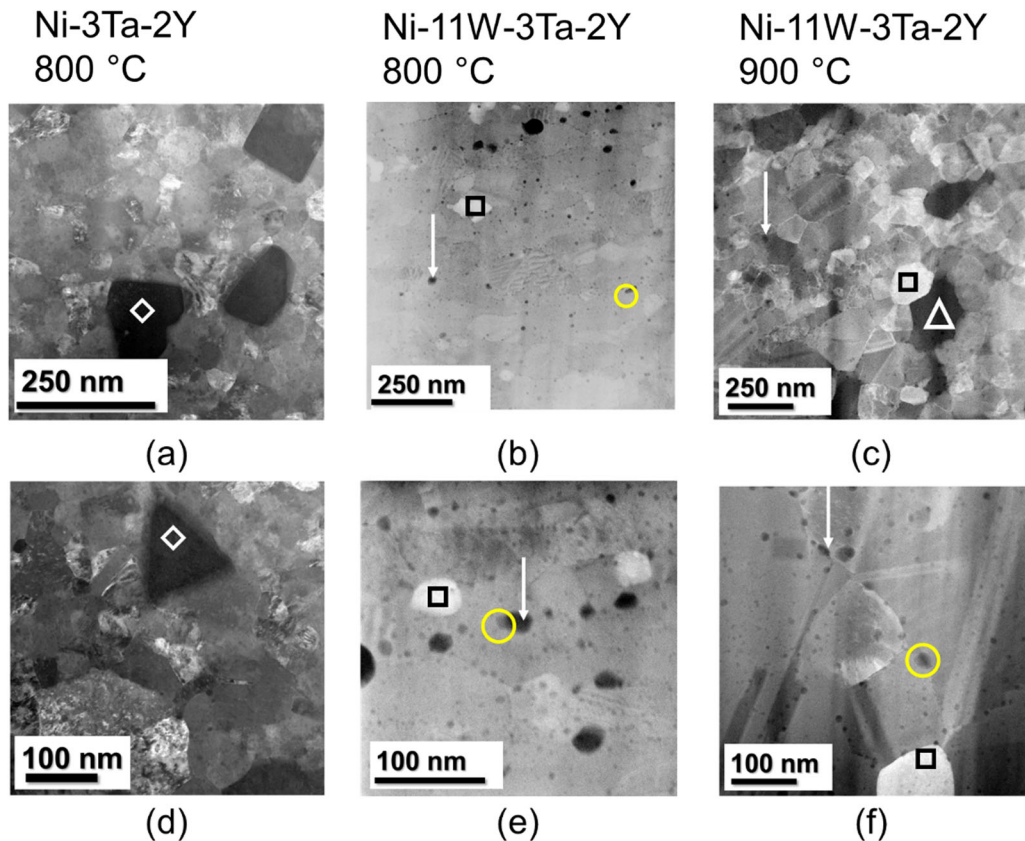


Fig. 5—STEM LAADF (a, c, d) and HAADF (b, e, f) images of samples annealed for 100 hours: Ni-3Ta-2Y at 800 °C (a, d), Ni-11W-3Ta-2Y at 800 °C (b, e), and Ni-11W-3Ta-2Y at 900 °C (c, f). In Ni-3Ta-2Y, YN particles are observed, which are not present in Ni-11W-3Ta-2Y due to the choice of cryogen for cryomilling; they are marked with white diamonds in images a and d. Pure W grains are marked with black squares and Ni<sub>3</sub>Y with white triangles. A large Y<sub>2</sub>O<sub>3</sub> particle is circled in yellow, and a large Ar bubble is marked with a white arrow in each image where they are visible. The LAADF micrographs were acquired using smaller collection angles than the other micrographs, giving rise to diffraction contrast (Color figure online).

XRD peak broadening and often yields falsely small grain sizes in cryomilled alloys. Figure 6(b) reveals the growth trends for the quaternary Ni system and binary Ni-1Y which both remained in the nanocrystalline regime for all heat treatments. The average grain sizes of Ni-11W-3Ta-2Y after annealing at 800 °C for 1 and 100 hours were within one standard deviation of each other,  $40.4 \text{ nm} \pm 5.6$  and  $38.7 \text{ nm} \pm 9.4 \text{ nm}$ , respectively, indicating thermal stability against grain coarsening. Darling *et al.* attribute the grain size stability of the Ni-Y system to the kinetic pinning of grain boundaries by YN particles which form due to cryomilling with liquid nitrogen.<sup>[19]</sup> In this study, the Ni-3Ta-2Y alloy was cryomilled using liquid nitrogen, but liquid argon was used as the cryogen in milling Ni-11W-3Ta-2Y, rather than liquid nitrogen. The alloyed pellets were annealed in argon, while Darling *et al.* annealed the Y-doped Ni samples in a slightly reducing Ar-2 pct H<sub>2</sub> gas.<sup>[19]</sup> Thus, rather than YN, Y<sub>2</sub>O<sub>3</sub> particles formed in the Ni-11W-3Ta-2Y alloy, but they appear to play a similar role in stabilizing the nanoscale grains for similar annealing treatments.

Vickers microhardness testing was performed to determine processing-structure-property relationships of the Ni alloys. The results comparing hardness values

after annealing each composition for 1 and 100 hours are presented in Figure 7. Vickers microhardness measurement from as-milled and annealed Ni-11W-3Ta-2Y are used to compare the hardness of this alloy to that of Ni-3Ta-2Y cryomilled with liquid nitrogen and subsequently compacted and annealed. The hardness values of the two alloys after annealing for 1 hour are similar for all annealing treatments, but following the 100 hours anneals, the hardness of Ni-11W-3Ta-2Y is significantly higher and more stable than that of Ni-3Ta-2Y. The Ni-3Ta-2Y and Ni-1Y alloys are stabilized by YN particles, while the Ni-11W-3Ta-2Y alloy is stabilized by grain boundary pinning from Y<sub>2</sub>O<sub>3</sub> particles. There is a severe drop in hardness of Ni-3Ta-2Y after annealing for 100 hours, from 6.1 GPa for the 800 °C anneal to 1.2 GPa for 1000 °C, compared to the much more gradual decrease in hardness of Ni-11W-3Ta-2Y for the same annealing treatments from 8.4 to 7.4 GPa. This indicates that, while the YN particles are able to stabilize the nanoscale grains significantly for shorter term anneals (1 hour), they are not as stable against coarsening or effective for longer term anneals (100 hours) as the Y<sub>2</sub>O<sub>3</sub> particles seen in the Ni-11W-3Ta-2Y samples.

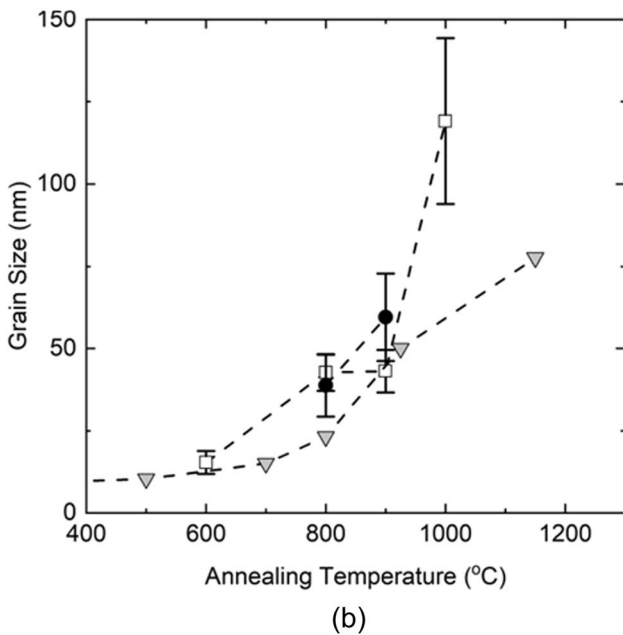
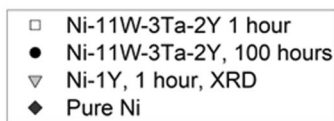
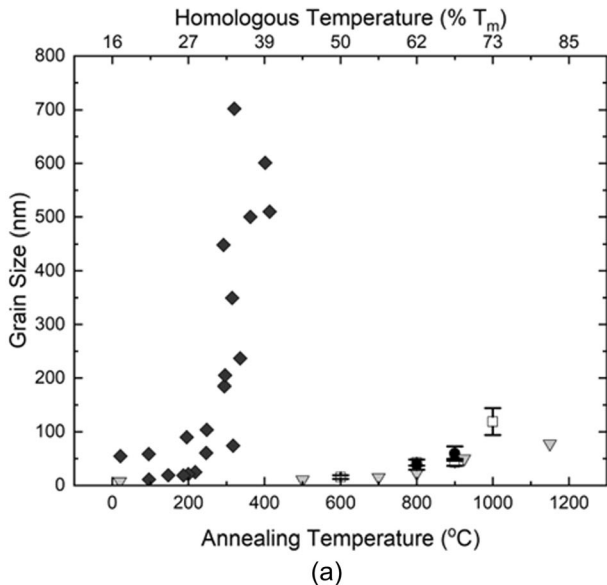


Fig. 6—(a) and (b). Grain size versus annealing temperature following one hour anneals; grain sizes following 100 hour anneals are also plotted for Ni-11W-3Ta-2Y. (a) compares pure nc-Ni to Ni-1Y and Ni-11W-3Ta-2Y. (b) contains only alloyed compositions on an enlarged y-axis to better visualize grain growth trends. The error bars in both plots indicate 2 standard deviations (95 pct confidence interval) on a normal distribution.

In addition, the hardness of Ni-11W-3Ta-2Y annealed at 800 °C for 100 hours was more than 2 GPa greater than that of Ni-3Ta-2Y annealed under the same conditions (Ni-11W-3Ta-2Y: 8.4 GPa, Ni-3Ta-2Y: 6.1 GPa). The grain sizes of both 800 °C, 100 hours annealed samples were measured using the line intercept method on STEM BF/LAADF images;

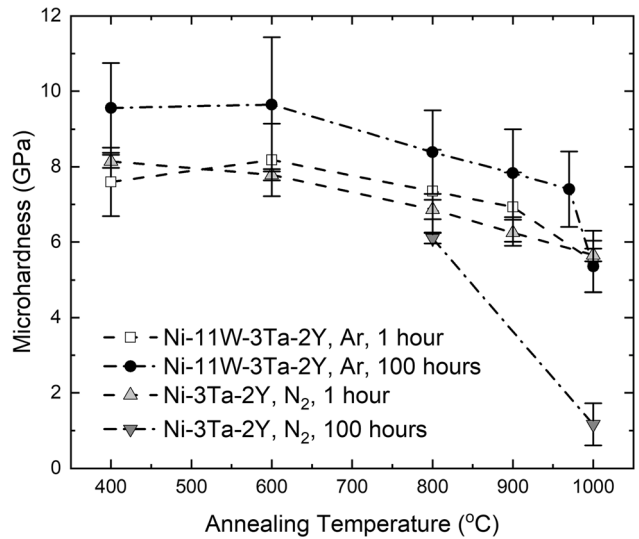


Fig. 7—Microhardness versus annealing temperature for 1 and 100 hour anneals, comparing the mechanical property evolution of Ni-11W-3Ta-2Y milled with liquid Ar to that of Ni-3Ta-2Y milled with liquid N<sub>2</sub>. Error bars represent 2 standard deviations (95 pct confidence) on a normal distribution.

Ni-11W-3Ta-2Y had an average grain size of  $38.7 \pm 9.4$  nm, while Ni-3Ta-2Y had an average grain size of  $44.2 \pm 7.8$  nm. The average grain sizes are similar, so the difference in average hardness between the two samples is beyond a simple Hall-Petch relationship; thus, the increase in hardness seen in the Ni-11W-3Ta-2Y alloy is due to a combination of strengthening effects from the dissolved W and Ta as well as secondary phases, including the Y<sub>2</sub>O<sub>3</sub> particles, Ni<sub>5</sub>Y intermetallics, and pure W and Ta grains that remain from milling.

## IV. DISCUSSION

### A. Microstructural Evolution

The microstructures observed in the Ni-11W-3Ta-2Y alloy after various annealing treatments have been stable against grain coarsening, made up primarily of a Ni-rich FCC phase containing dissolved W and Ta. After annealing for 1 hour, pure W and intermetallic Ni<sub>4</sub>W are observed based on SAED analysis, and large W and Ta grains are observed in STEM HAADF imaging with compositions confirmed using EDS. The pure W/Ta grains are artifacts from particles that did not mix fully during milling. After annealing at high temperatures and for longer times, intermetallic Ni<sub>5</sub>Y is observed in EDS analysis and STEM micrographs, as seen in Figures 2, 4, and 5. A small amount of pure W and Ta grains as unmixed phases remnant from milling are also seen in STEM micrographs of longer-term-annealed samples in Figure 5, marked by black squares. These pure W and Ta grains are initially large in the sample annealed at 600 °C for 1 hour (Figures 4(b) and (g)), but once annealed at higher temperatures or for longer times the W and Ta diffuse and dissolve into the Ni phase. The 11 at pct W and 3 at pct Ta that were

intended to dissolve into the Ni-rich FCC phase during annealing were both added to assist with the high-temperature strength of this phase; W and Ta reduce the stacking fault energy of Ni,<sup>[3]</sup> so they should promote the formation of partial dislocations and twins, increasing the strength of the alloy. In addition, all samples were found to contain Y<sub>2</sub>O<sub>3</sub>, as some oxygen contamination is inevitable in powder processing. Typically found along grain boundaries and coupled with the Y<sub>2</sub>O<sub>3</sub> particles, Ar bubbles were found in all samples when characterized *via* STEM; they are an artifact and were introduced when the powder was loaded into the milling vials inside of the Ar-filled glovebox. Some Ar is inevitably trapped inside of the vial when it is capped, and then the captured Ar is condensed and dispersed throughout the powder during cryomilling.

Yttrium was considered as an oxygen getter, due to the lower free energy of formation of yttrium oxide compared to all other possible oxides in this system (Ni, Ta, and W-based oxides),<sup>[36,37]</sup> which helps keep the tungsten dissolved in the Ni-rich phase rather than forming W oxides. W-based oxides have been found in the binary Ni–W alloys.<sup>[38,39]</sup> While no oxygen was intentionally added to the system, it was likely introduced by surface oxides on the initial elemental powders. During mechanical alloying, sufficient mechanical energy may be provided to the system to induce chemical reactions despite the low temperature,<sup>[40]</sup> allowing the yttrium powder particles to reduce all other surface oxides mechanochemically.<sup>[41]</sup>

In addition to tying up any oxygen contamination, these yttrium oxide particles play a significant role in stabilizing the microstructure *via* grain boundary pinning, similar to the Ta-based nanoparticles in the Cu-Ta system. Based on STEM imaging of long-term anneals, the Y<sub>2</sub>O<sub>3</sub> particle size is stable, with the average particle diameter only coarsening from 5.7 to 7.6 nm after annealing at 900 °C for 1 and then 100 hours. They remain in the 10 nm range in this system, so they are capable of stabilizing against grain growth for the annealing times and temperatures studied in this work.

While several stabilization phenomena have been reported in nanocrystalline materials, the enhanced stability of nanocrystalline Ni–11W–3Ta–2Y is dominated by pinning of grain boundaries by Y<sub>2</sub>O<sub>3</sub> particles and Ar bubbles.<sup>[18]</sup> Hallmarks of other stabilization mechanisms (such as solute segregation or grain boundary complex formation) have not been observed in grain boundary EDS measurements where no grain boundary segregation was found.

Following Doherty *et al.*'s model for grain boundary pinning, the limiting mean grain radius,  $R$ , is given by Equation [1]<sup>[42]</sup>:

$$R = r \sqrt{\frac{\pi}{2\beta\phi f}} \quad [1]$$

where  $r$  is the average particle radius,  $\beta$  is a factor of curvature relating the average grain boundary radius of curvature to the average grain radius and commonly taken to be 2,  $\phi$  is the fraction of particles that are at the

grain boundaries, and  $f$  is the volume fraction of particles as measured from a 2D image.

Using the average Y<sub>2</sub>O<sub>3</sub> particle diameter, area fraction, and fraction that are at grain boundaries measured from STEM images, the limiting grain diameter was estimated for samples annealed at 900 °C for 1 and 100 hours to be 32.7 and 52.1 nm, respectively. The parameters used in this calculation were measured from three random 500 nm × 500 nm areas for each annealing treatment, and they are presented in Table I. These expected values are slightly smaller than the 43.1 nm (900 °C 1 hour) and 59.5 nm (900 °C 100 hours) average grain diameters measured using the line intercept method for these samples, at  $-1.6\sigma$  and  $-0.6\sigma$ , respectively. This analysis also neglected the potential pinning effects of the Ar bubbles, which also sit at grain boundaries and may play an additional pinning role, limiting the grain sizes further to 20.2 and 33.5 nm when both Y<sub>2</sub>O<sub>3</sub> particles and Ar bubbles are considered together.

Pinning models, including Doherty's model used in this analysis as well as the commonly used Zener pinning model, assume that the particles are immobile, inert, and perfectly stable against coarsening. In this system, the Y<sub>2</sub>O<sub>3</sub> particles and Ar bubbles are observed to both move and coarsen during annealing. While their degree of coarsening is limited, with the Y<sub>2</sub>O<sub>3</sub> particles only growing from 5.7 nm after annealing at 900 °C for 1 hour to 7.6 nm after annealing at 900 °C for 100 hours, and Ar bubbles from 3.3 to 5.8 nm for the same annealing conditions, this growth still likely affects the pinning forces they exert on grain boundaries. The average measured grain sizes are within range of the limiting grain size predicted by Doherty's model, and the particle mobility and growth may contribute to a larger limiting grain size than predicted by models. It is reasonable that this grain boundary-pinning model does not perfectly capture the behavior observed in the Ni–11W–3Ta–2Y alloy because its assumptions about the nature of the pinning particles are not met in this system, but it still serves as a means of better understanding the particles' role in the observed thermal stability.

## B. Hardness Stability and Mechanical Properties

Microstructural stability of nanoscale grains after short- and long-term high-temperature anneals also supports the stability of the alloy's mechanical properties. When comparing the hardness evolution of Ni–11W–3Ta–2Y to that of Ni–3Ta–2Y following 1 and 100 hours anneals, the temperature-based evolution for 1 hour anneals appear similar between the two alloys. However, after annealing for 100 hours, Ni–3Ta–2Y had lower hardness values for both of the measured temperatures (800 and 1000 °C), in addition to a significant drop in hardness from 800 (6.1 GPa) to 1000 °C (1.2 GPa). After annealing Ni–11W–3Ta–2Y for 100 hours, the hardness for each annealing temperature was *higher* than that of the Ni–11W–3Ta–2Y samples annealed for 1 hour at the same respective temperature. The as-milled powder compacts may have



**Table I. Calculated Limiting Grain Radius and Relevant Parameters for Ni-11W-3Ta-2Y Annealed at 900 °C for 1 and 100 Hours, Considering the Pinning Effects of Y<sub>2</sub>O<sub>3</sub> Particles Alone and Together with Ar Bubbles**

Annealing Treatment	Particle Type Considered	$\beta$	Average Particle Radius (nm)	Area Fraction Particles	Fraction of Particles at Grain Boundaries	Limiting Grain Diameter (nm)
900 °C 1 h	Y <sub>2</sub> O <sub>3</sub> only	2	5.7 ± 2.9	0.066 ± 0.02	0.48 ± 0.05	32.7 ± 21
900 °C 1 h	Y <sub>2</sub> O <sub>3</sub> and Ar bubbles	2	4.5 ± 3.1	0.11 ± 0.03	0.47 ± 0.15	20.2 ± 17
900 °C 100 h	Y <sub>2</sub> O <sub>3</sub> only	2	7.6 ± 4.1	0.052 ± 0.05	0.43 ± 0.05	52.1 ± 39
900 °C 100 h	Y <sub>2</sub> O <sub>3</sub> and Ar bubbles	2	6.7 ± 5.1	0.095 ± 0.05	0.44 ± 0.15	33.5 ± 33

been partially amorphous, as is commonly observed in mechanically alloyed materials.<sup>[41]</sup> Crystallization occurred due to annealing, so the increase in hardness following the 100 hours anneals compared to the 1 hour anneals can be attributed to increased crystallinity.

Because the grains in Ni-11W-3Ta-2Y remained stable and nanoscale after annealing at 1000 °C for 100 hours, its more gradual decrease in hardness following 100 hours anneals compared to Ni-3Ta-2Y is likely due to a combination of the dissolved W and Ta increasing the high temperature strength and the Y<sub>2</sub>O<sub>3</sub> particles increasing the microstructural stability. The YN particles observed in Ni-3Ta-2Y exhibited angular morphologies and were more susceptible to coarsening than the Y<sub>2</sub>O<sub>3</sub> particles observed in Ni-11W-3Ta-2Y. STEM HAADF micrographs of both alloys after annealing at 800 °C for 100 hours are presented in Figures 5(b) and (e), showing the difference in particle size and morphology between the two alloys and cryogenics used. Following this long-term anneal, several of the YN particles in Ni-3Ta-2Y had coarsened to 50-170 nm, while the largest observed Y<sub>2</sub>O<sub>3</sub> particles in Ni-11W-3Ta-2Y only had a diameter of 21.7 nm. As the particle size  $r$  (in Equation [1]) increases, the particles exert a smaller pinning force against grain boundaries and are less effective at pinning them, thus increasing the limiting grain size,  $R$  (in Equation [1]).<sup>[42]</sup> It directly follows that the grains themselves in Ni-3Ta-2Y coarsen much more readily than in Ni-11W-3Ta-2Y because the systems' pinning particles coarsen at vastly different rates.

In addition to its enhanced microstructural stability, Ni-11W-3Ta-2Y demonstrated enhanced hardness *beyond what is expected based on grain size alone*. The expected hardness based on Hall-Petch hardening was calculated for Ni-11W-3Ta-2Y annealed at 1 and 100 hours, based on measured grain sizes and Hall-Petch coefficients published for nanocrystalline Ni-3-17 at pct W.<sup>[43]</sup> The difference between the measured hardness values and those expected based on grain size for a Ni-W solid solution is plotted in Figure 8, which displays the increase in hardness due to any secondary phases present. The measured hardness values of all annealed Ni-11W-3Ta-2Y samples were more than 2 GPa greater than the hardness expected due to

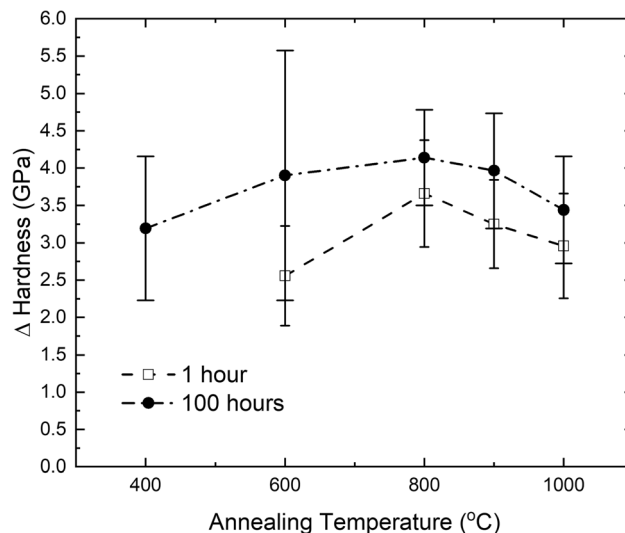


Fig. 8—Difference between measured microhardness values and Hall-Petch-based hardness estimates. Grain sizes were measured using the line intercept method on STEM LAADF images and Ni Hall-Petch coefficients from the literature<sup>[20]</sup> were used to calculate expected hardness values. Error bars indicate 95 pct confidence intervals on a normal distribution (two standard deviations).

Hall-Petch in Ni-W alloys for all annealing conditions, and for the long-term annealing condition, the measured hardness was 3 GPa greater than the expected value. The large amount of W dissolved in the Ni phase may contribute some solid-solution strengthening. However, this effect is negligible in the hardness of nanocrystalline Ni-W alloys<sup>[45,44]</sup>; Schuh *et al.* calculated that, for Ni with 14.1 at pct W dissolved in it, the solid-solution strengthening contribution to hardness is only approximately 40 MPa, while the intrinsic hardness of pure nickel is 800 MPa.<sup>[44]</sup> A similar effect was observed by Darling *et al.* in the Ni-Y system, in which the authors attributed the enhanced hardness to the YN particles.<sup>[19]</sup> The large enhancement in hardness indicates that the secondary phases, including Y<sub>2</sub>O<sub>3</sub> or YN particles, Ni<sub>5</sub>Y, and W and Ta grains that were not fully milled, play a role in strengthening this alloy in addition to Hall-Petch and solid-solution strengthening.

**Table II. Estimated Hardness and Relevant Parameters for Ni–11W–3Ta–2Y Annealed at 900 °C for 1 and 100 Hours, Considering a Rule of Mixtures for the Solid Solution (Matrix) and Secondary Phases, Hall–Petch Strengthening, Orowan Looping Around Y<sub>2</sub>O<sub>3</sub> Particles, and the Contribution of Porosity**

	900 °C 1 h	900 °C 100 h
$H_{\text{FCC}}$ (GPa) <sup>[44]</sup>	2.15 ± 0.7	2.16 ± 0.7
$f_{\text{FCC}}$	0.76 ± 0.06	0.80 ± 0.02
$H_{\text{Ni5Y}}$ (GPa) <sup>[47]</sup>	6.89	6.89
$f_{\text{Ni5Y}}$	0.07 ± 0.008	0.07 ± 0.01
$H_{\text{W}}$ (GPa) <sup>[48]</sup>	4.02	4.02
$f_{\text{W}}$	0.06 ± 0.02	0.03 ± 0.008
$H_{\text{Ta}}$ (GPa) <sup>[49]</sup>	0.88	0.88
$f_{\text{Ta}}$	0.007 ± 0.002	0.009 ± 0.007
$H_{\text{Hall–Petch}}$ <sup>[3]</sup>	3.20 ± 0.4	2.84 ± 0.6
$H_{\text{Orowan Looping}}$ <sup>[3]</sup>	5.62 ± 1.6	4.68 ± 2.2
$b$	8	8
$P$	0.044 ± 0.007	0.037 ± 0.02
$H_{\text{est}}$ (GPa)	<i>7.81 ± 1.8</i>	<i>7.33 ± 2.4</i>
$H_{\text{measured}}$ (GPa)	<i>7.89 ± 0.9</i>	<i>7.83 ± 1.2</i>

Italic values indicate to differentiate measured hardness from parameters used within the calculation of the estimated hardness

The details of the strengthening mechanisms augmenting the Hall–Petch contribution are the subject of future work; however, preliminary calculations support their additional strengthening role. Equation [2] estimates the hardness of a material when multiple strengthening mechanisms are present using a rule of mixtures-type calculation coupled with an exponential term to describe the contributions of porosity, including argon bubbles.<sup>[45]</sup> The hardness of the FCC phase in this calculation includes solid-solution strengthening from W and Ta dissolved in the Ni, as measured using EDS.<sup>[46]</sup> In this estimation, due to the size, spacing, and relative hardness of the Y<sub>2</sub>O<sub>3</sub> particles compared to the Ni matrix, it is assumed that dislocations loop around them rather than shearing through the particles.

$$H_{\text{est}} = \left( H_{\text{FCC}}f_{\text{FCC}} + \sum H_{\text{2nd phase}}f_{\text{2nd phase}} + H_{\text{H–P}} + H_{\text{Orowan}} \right) \exp(-bP), \quad [2]$$

where  $H_{\text{est}}$  is the estimated overall Vicker’s hardness in GPa,  $f_{\text{FCC}/\text{2ndPhase}}$  is the volume fraction of a particular phase,  $H_{\text{FCC}/\text{2ndPhase}}$  represents the bulk hardness of a particular phase,  $H_{\text{Hall–Petch}}$  is the hardness contribution due to grain size effects,  $H_{\text{Orowan}}$  is the contribution due to dislocation looping around Y<sub>2</sub>O<sub>3</sub> particles,  $P$  is the volume fraction of porosity, or in the case of this experiment, argon bubbles, and  $b$  is a material-dependent constant associated with porosity that varies between 2 and 8. The results of applying this calculation to the Ni–11W–3Ta–2Y samples annealed at 900 °C for 1 and 100 hours are presented in Table II along with the parameters used.

## V. CONCLUSIONS

High-energy cryogenic mechanical alloying of Ni with two miscible solutes, 11 at pct W, 3 at pct Ta, and one immiscible component, 2 at pct Y, resulted in a nanocrystalline alloy with a microstructure that is increasingly stabilized against coarsening. Kinetic-based stability of the alloy is demonstrated after annealing at a high temperature (67–73 pct homologous temperature) for a longer time (100 hours) than is typically studied. The stability of this alloy is attributed to kinetic pinning of grain boundaries by stable Y<sub>2</sub>O<sub>3</sub> particles and Ar bubbles. Both alloys studied, Ni–3Ta–2Y cryomilled with liquid nitrogen and Ni–11W–3Ta–2Y cryomilled with liquid argon, exhibit excellent hardness which is enhanced even beyond simple Hall–Petch strengthening, due to a precipitation hardening-like behavior related to the secondary phases (Y<sub>2</sub>O<sub>3</sub>, Ni<sub>5</sub>Y, and unmixed W and Ta) present in this system. While contamination is inevitable in mechanical alloying and is often designed around when selecting alloy components, in this work, contamination was exploited to form beneficial secondary phases that improved both the stability and hardness of the nanocrystalline alloys.

## ACKNOWLEDGMENTS

Research was sponsored by the Army Research Laboratory and was accomplished under Cooperative Agreement Number W911NF-22-2-0032 titled Lightweight High Entropy Alloy Design (LHEAD) Project. The views and conclusions contained in this document are those of the authors and should not be interpreted as representing the official policies, either expressed or implied, of the Army Research Office or the U.S. Government. The U.S. Government is authorized to reproduce and distribute reprints for Government purposes notwithstanding any copyright notation herein. In addition, the authors would like to acknowledge the support of the Lehigh University Nano|Human Interfaces Presidential Initiative as well as the National Defense Science and Engineering Graduate (NDSEG) Fellowship Program.

## CONFLICT OF INTEREST

On behalf of all authors, the corresponding author states that there is no conflict of interest.

## DATA AVAILABILITY

The raw and processed data required to reproduce these findings are available upon request.

## APPENDIX

See Figure A1.

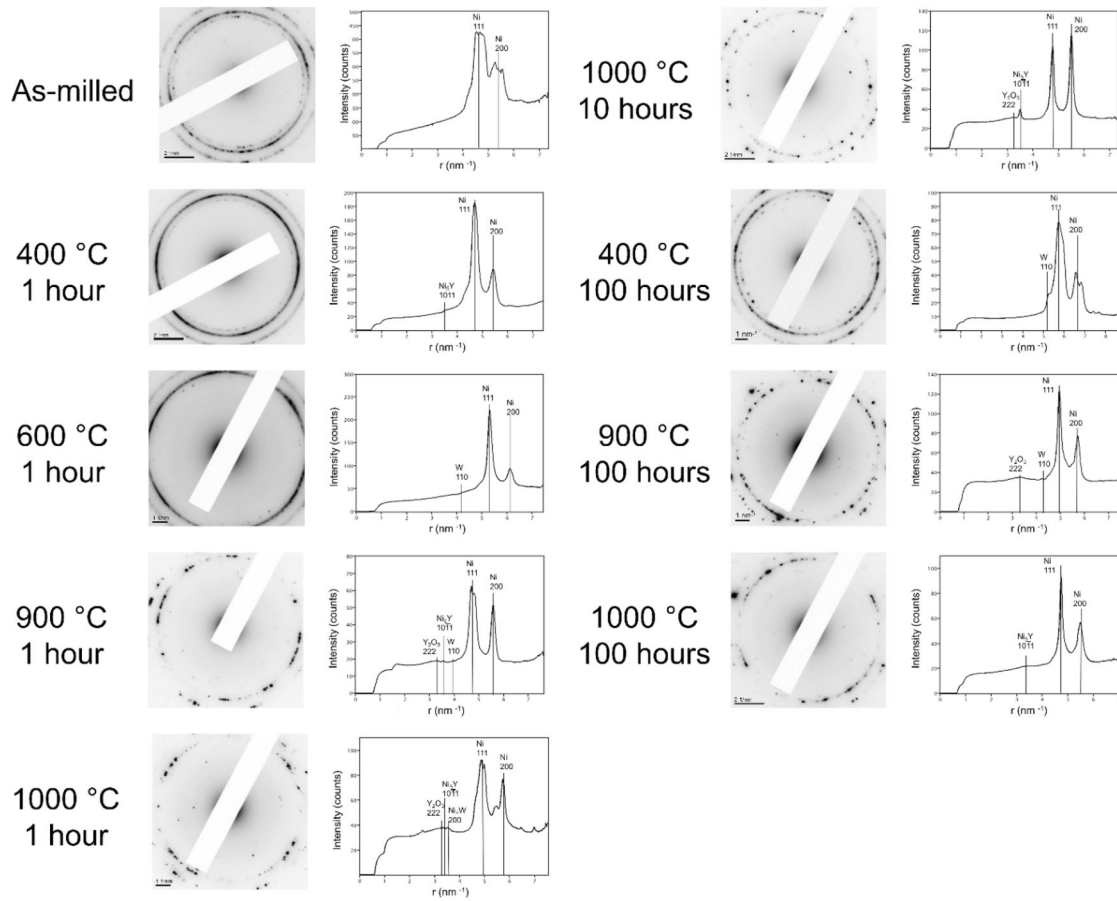


Fig. A1—Representative full SAED patterns and associated Azimuthal projections that were used to aid phaseidentification in Ni-11W-3Ta-2Y samples in the as-milled and annealed conditions. Sections of these SAED patterns were cropped and presented in Figure 1 with the spots labeled.

See Figure A2.

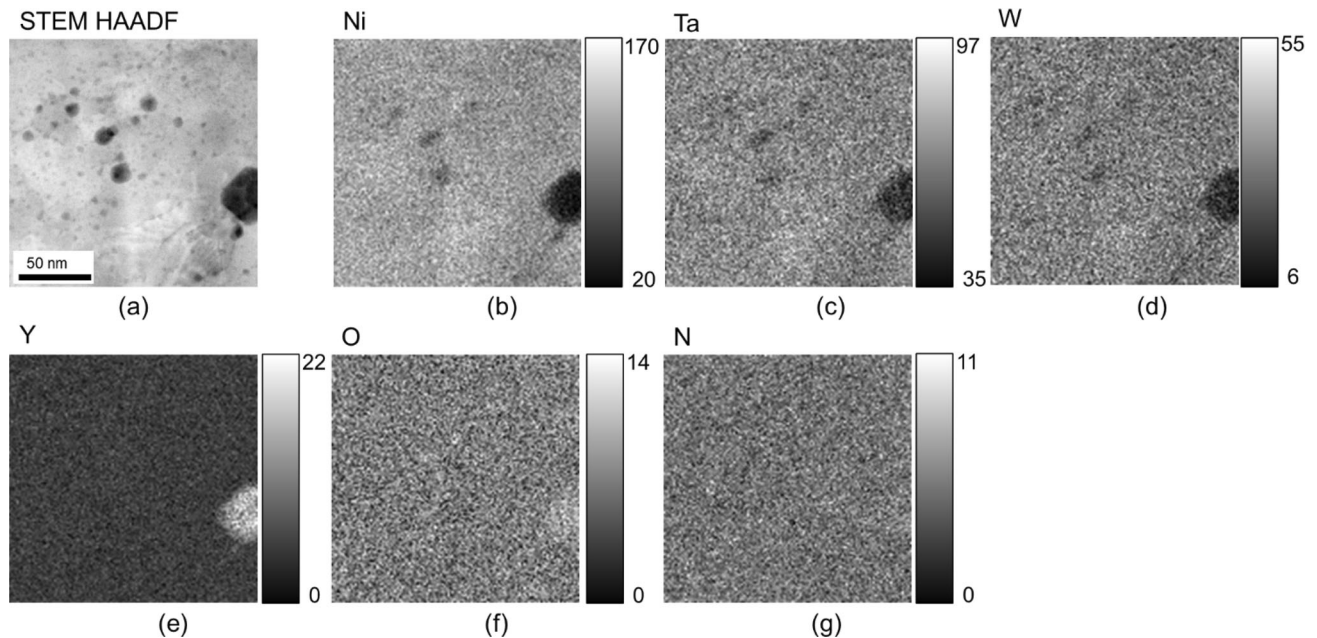


Fig. A2—STEM HAADF micrograph (a) and STEM EDS elemental maps (b–g) of a representative area of the Ni-11W-3Ta-2Y sample annealed at 800 °C for 100 hours at a higher magnification than Figure 2. A large particle that is enriched in both Y and O and depleted in Ni, Ta, and W is seen in the right side of the micrograph and EDS maps. By combining EDS measurements and SAED patterns, this phase was identified as  $Y_2O_3$ . The surrounding matrix phase is observed to contain Ni, W, and Ta.

## REFERENCES

1. E.O. Hall: *Proc. Phys. Soc. Sect. B*, 1951, vol. 64, pp. 747–53.
2. N.J. Petch: *J. Iron Steel Inst.*, 1953, vol. 174, pp. 25–28.
3. G.E. Dieter: *Mechanical Metallurgy*, 3rd ed. McGraw-Hill, New York, 1986.
4. C. Suryanarayana: *Nanocryst. Mater.*, 1995, pp. 161–93.
5. G.D. Hibbard, V. Radmilovic, K.T. Aust, and U. Erb: *Mater. Sci. Eng. A*, 2008, vol. 494, pp. 232–38.
6. T. Chookajorn and C.A. Schuh: *Phys. Rev. B*, 2014, vol. 89, pp. 1–10.
7. J.R. Trelewicz and C.A. Schuh: *Phys. Rev. B*, 2009, vol. 79, pp. 1–13.
8. T. Chookajorn, H.A. Murdoch, and C.A. Schuh: *Science (80-)*, 2012, vol. 337, pp. 951–54.
9. C.C. Koch, R.O. Scattergood, K.A. Darling, and J.E. Semones: *J. Mater. Sci.*, 2008, vol. 43, pp. 7264–72.
10. K.A. Darling, B.K. VanLeeuwen, J.E. Semones, C.C. Koch, R.O. Scattergood, L.J. Kecskes, and S.N. Mathaudhu: *Mater. Sci. Eng. A*, 2011, vol. 528, pp. 4365–71.
11. A. Khalajhedayati and T.J. Rupert: *JOM*, 2015, vol. 67, pp. 2788–2801.
12. J.D. Schuler, O.K. Donaldson, and T.J. Rupert: *Scr. Mater.*, 2018, vol. 154, pp. 49–53.
13. T.J. Rupert: *Curr. Opin. Solid State Mater. Sci.*, 2016, vol. 20, pp. 257–67.
14. N. Zhou, T. Hu, J. Huang, and J. Luo: *Scr. Mater.*, 2016, vol. 124, pp. 160–63.
15. C.M. Grigorian and T.J. Rupert: *Acta Mater.*, 2019, vol. 179, pp. 172–82.
16. P. Gao, S. Sun, H. Li, R. Niu, S. Han, H. Zong, H. Wang, J. Lian, and X. Liao: *J. Mater. Sci. Technol.*, 2022, vol. 106, pp. 1–9.
17. A.R. Kalidindi and C.A. Schuh: *Acta Mater.*, 2017, vol. 132, pp. 128–37.
18. J.A. Smeltzer, C.J. Marvel, B.C. Hornbuckle, A.J. Roberts, J.M. Marsico, A.K. Giri, K.A. Darling, J.M. Rickman, H.M. Chan, and M.P. Harmer: *Mater. Sci. Eng. A*. <https://doi.org/10.1016/j.msea.2019.138140>.
19. K.A. Darling, L.J. Kecskes, M. Atwater, J. Semones, R.O. Scattergood, and C.C. Koch: *J. Mater. Res.*, 2013, vol. 28, pp. 1813–19.
20. B.C. Hornbuckle, K. Solanki, and K.A. Darling: *Mater. Sci. Eng. A*. <https://doi.org/10.1016/j.msea.2021.141818>.
21. K.A. Darling, A.J. Roberts, Y. Mishin, S.N. Mathaudhu, and L.J. Kecskes: *J. Alloys Compd.*, 2013, vol. 573, pp. 142–50.
22. T. Frolov, K.A. Darling, L.J. Kecskes, and Y. Mishin: *Acta Mater.*, 2012, vol. 60, pp. 2158–68.
23. C.J. Marvel, B.C. Hornbuckle, J.A. Smeltzer, K.A. Darling, and M.P. Harmer: *Scr. Mater.*, 2020, vol. 188, pp. 69–73.
24. K.A. Darling, M. Rajagopalan, M. Komarasamy, M.A. Bhatia, B.C. Hornbuckle, R.S. Mishra, and K.N. Solanki: *Nature*. <https://doi.org/10.1038/nature19313>.
25. L. Raman, K. Gothandapani, and B.S. Murty: *Def. Sci. J.*, 2016, vol. 66, pp. 316–22.
26. P. Nash, ed.: *Phase Diagrams of Binary Nickel Alloys*, ASM International, Materials Park, OH, 1991.
27. J.C. Slater: *J. Chem. Phys.*, 1964, vol. 41, pp. 3199–204.
28. B. Cordero, V. Gómez, A.E. Platero-Prats, M. Revés, J. Echeverría, E. Cremades, F. Barragán, and S. Alvarez: *J. Chem. Soc. Dalton Trans.*, 2008, pp. 2832–38.
29. P. Pykkö and M. Atsumi: *ChemistryEurope*, 2009, vol. 15, pp. 186–97.
30. P.C.J. Gallagher: *Metall. Trans.*, 1970, vol. 1, pp. 2429–61.

31. J.M. Bai, H.P. Zhang, J.T. Liu, Q.S. Sun, C.S. Liu, and Y.W. Zhang: *Mater Charact*, 2022, vol. 191, 112089.
32. G. Sharma, J. Varshney, A.C. Bidaye, and J.K. Chakravarty: *Mater. Sci. Eng. A*, 2012, vol. 539, pp. 324–29.
33. M.C. Iordache, S.H. Whang, Z. Jiao, and Z.M. Wang: *Nanos-structured Mater.*, 1999, vol. 11, pp. 1343–49.
34. H. Natter, M. Schmelzer, and R. Hempelmann: *J. Mater. Res.*, 1998, vol. 13, pp. 1186–97.
35. Standard Test Methods for Determining Average Grain Size (ASTM International: 2021), <https://compass.astm.org/document/?contentCode=ASTM%7CE0112-13R21%7Cen-US>. Accessed 01 November, 2023.
36. T.B. Reed: *Free Energy of Formation of Binary Compounds*, MIT Press, Cambridge, MA, 1971.
37. S.M. Howard, Ellingham Diagrams. (South Dakota School of Mines and Technology, 2006), [http://showard.sdsmt.edu/ME T320/Handouts/EllinghamDiagrams/Ellingham\\_v22\\_Macro.pdf](http://showard.sdsmt.edu/ME T320/Handouts/EllinghamDiagrams/Ellingham_v22_Macro.pdf). Accessed 01 November, 2023.
38. W. Cao, C. Marvel, D. Yin, Y. Zhang, P. Cantwell, M.P. Harmer, J. Luo, and R.P. Vinci: *Scr. Mater.*, 2016, vol. 113, pp. 84–88.
39. C.J. Marvel: *J. Mater. Sci.*, 2019, vol. 54, pp. 3496–508.
40. S. Mateti, M. Mathesh, Z. Liu, T. Tao, T. Ramireddy, A.M. Glushenkov, W. Yang, and Y.I. Chen: *Chem. Commun.*, 2021, vol. 57, pp. 1080–92.
41. C. Suryanarayana: *Mech. Alloy. Milling*, 2004, vol. 46, pp. 1–472.
42. R.D. Doherty, D.J. Srolovitz, A.D. Rollett, and M.P. Anderson: *Scr. Metall.*, 1987, vol. 21, pp. 675–79.
43. D. Yin, Microstructure and Microcantilever Fracture Toughness of Electrodeposited Ni-W Alloys (Lehigh University, 2017), <http://preserve.lib.lehigh.edu/islandora/object/preserve%3AAbp-10370186>. Accessed 1 November, 2023.
44. C.A. Schuh, T.G. Nieh, and H. Iwasaki: *Acta Mater.*, 2003, vol. 51, pp. 431–43.
45. J.A. Smeltzer, M.T. Burton, B.C. Hornbuckle, A.K. Giri, K.A. Darling, M.P. Harmer, and C.J. Marvel: *Mater. Des.*, 2021, vol. 210, 110070.
46. T.J. Rupert, J.C. Trenkle, and C.A. Schuh: *Acta Mater.*, 2011, vol. 59, pp. 1619–31.
47. Y.X. Zhou, M.Y. Hu, P. Yan, X. Shi, X.Y. Chong, and J. Feng: *RSC Adv.*, 2018, vol. 8, pp. 41575–86.
48. J.H. Yu, H. Tanigawa, D. Hamaguchi, and T. Nozawa: *Fusion Eng. Des.*, 2020, vol. 157, 111679.
49. S. Nasser: *Materials for Medical Devices*, vol. 23, 2012.

**Publisher's Note** Springer Nature remains neutral with regard to jurisdictional claims in published maps and institutional affiliations.

Springer Nature or its licensor (e.g. a society or other partner) holds exclusive rights to this article under a publishing agreement with the author(s) or other rightsholder(s); author self-archiving of the accepted manuscript version of this article is solely governed by the terms of such publishing agreement and applicable law.